A novel approach in mechanical nanostructuring synthesis of metal hydride: Hydrogen sorption enhancement by High Pressure Torsion Extrusion

Babak Omranpour Shahreza [a,b,c,*], Julia Ivanisenko [d], Fjodor Sergejev [b], Hosseinali Omranpour [e], Jacques Huot [a]

[a] Hydrogen Research Institute, University of Quebec in Trois-Rivieres (UQTR), 3351 des Forges, Trois-Rivieres, G9A 5H7, Canada
[b] Department of Mechanical and Industrial Engineering, Tallinn University of Technology (TalTech), Ehitajate tee 5, Tallinn, 19086, Estonia
[c] Department of Chemical and Materials Engineering, Complutense University of Madrid (UCM), Av. Complutense, 28040, Madrid, Spain
[d] Institute of Nanotechnology (INT), Karlsruhe Institute of Technology (KIT), 76021, Karlsruhe, Germany
[e] Department of Mechanical and Industrial Engineering, University of Toronto, Toronto, Ontario, Canada, M5S 3G8

ARTICLE INFO

ABSTRACT

In this study, we evaluated the influence of a new mechanical nanostructuring technique called High Pressure Torsion Extrusion (HPTE) on the microstructural evolution of niobium and the subsequent effects on the mechanical properties and hydrogen storage behaviour. Two different regimes with the extrusion speeds of $\nu = 7$ mm/min and $\nu = 10$ mm/min were implemented in the experiments. A remarkable microstructural refinement and increase in hardness were achieved after one pass of HPTE. The initial grain size of 16.5 μm decreased to 600 nm and the initial hardness of 80 Hv increased to 284 Hv. Using a Sievert apparatus, it was found that the HPTE processed sample could absorb hydrogen to its full capacity within about 6 h while the as-received sample did not absorb even after one day of exposure to hydrogen gas. Rate limiting step modelling of the hydrogen absorption revealed that the absorption is a 3-dimensional diffusion-controlled reaction with a constant or decreasing interface velocity, depending on the HPTE regime.

1. Introduction

Environmental pollution and fossil fuel depletion are the main issues that compel scientists to search for clean energy resources for the future [1]. Hydrogen is an efficient energy vector since the only by-product of combustion is water which can be reused again to produce hydrogen. In addition, hydrogen can generate a large amount of energy per unit volume during combustion [2]. However, the storage and transportation of hydrogen are the major obstacles to the development of hydrogen technology [3]. The gaseous and liquid storage of hydrogen are the common ways of storage though not very efficient in many applications due to the requirements of using high pressures for gas storage or the cryogenic temperatures associated with liquid storage [4]. Metal hydrides as a solid-state form of hydrogen storage have proved to be a practical solution to the conventional methods [5]. They can reversibly operate at low pressures of less than 100 bar as compared with 300–700 bar pressurized tanks [6]. In addition, they offer high volumetric density

of storage ($\sim$150 kg/m^3) [7]. Safety is another important aspect of metal hydrides; in case of severe crash accidents, there is no chance of detonation of hydrogen because hydrogen atoms are chemically bound to the metal atoms [8]. Nevertheless, there are some drawbacks. One of the main obstacles restricting the utilization of metal hydrides is the first hydrogenation which is usually very slow because the surface of the material is covered with oxides and other impurities; so, the alloy has to be operated at high temperatures and pressures to break these barriers and let hydrogen diffuse into the material. As a result, the final synthesized hydride will be costly [9]. Some remedies, however, are available to fix these deficiencies. First, increasing the surface-to-volume ratio may help to raise the chance of exposure of the specimens to hydrogen gas and thus, increase the sorption kinetics [10]. Another solution is introducing catalysts into the metal hydrides that could accelerate the dissociative sorption and associative desorption of hydrogen molecules [11]. Further, implementing mechanical nanostructuring techniques such as Severe Plastic Deformations (SPD) [12]

could help to facilitate hydrogen sorption by refining the microstructure [13,14]. Mechanical nanostructuring methods, in general, have two major impacts on metal hydrides. Firstly, they can induce crystalline defects in materials [15]. These defects act as nucleation points for the hydrogenation reactions [16]. Secondly, mechanical nanostructuring techniques help to reduce the grain size in metals and accordingly increase the density of the grain boundaries [17]. These boundaries act as a gateway for the hydrogen atoms to diffuse into the material, hence accelerating the kinetics of hydrogenation [10]. Additionally, imposing large shear strains can be useful for synthesizing materials from immiscible systems [18].

Several SPD techniques have been used so far to enhance the mechanical and functional properties of materials including the enhancement of hydrogenation kinetics. Some of the most famous ones can be named as Equal Channel Angular Pressing (ECAP) [19,20], Indirect Extrusion Angular Pressing (IEAP) [21,22], Fast Forging [23], Shot peening [24], High Pressure Torsion (HPT) [25], Accumulative Roll Bonding (ARB) [26], Twist Extrusion (TE) [27], Hard Cyclic Viscoplastic Deformation (HCVD) [28,29], Cyclic Expansion and Extrusion (CEE) [30], and so on. High Pressure Torsion Extrusion (HPTE) as a new-emerging technique has proved to be effective in the microstructural refinement of materials such as copper [31] and aluminum [32]. However, the effect of the process parameters on the functional properties of materials such as the hydrogenation and the kinetics of hydrogen sorption has not been studied yet. Our preliminary study on the comparison of HPTE and ECAP showed that HPTE was more effective in improving the kinetics of the first hydrogenation in niobium [33]. Niobium can form an epsilon-phase (ɛ) metal hydride at room temperature which acts as a gateway for hydrogen to transform and thus, decreases the energy barrier in the hydrogenation/dehydrogenation of other metals (such as magnesium) [34]. Niobium is quite ductile, making it possible to easily deform it by imposing large amounts of strain [22]. In this paper, we will be reporting the effect of HPTE on the microstructure and hydrogen-sorption properties of niobium, and we will study the mechanism of absorption using the regression analysis of Rate Limiting Step.

2. Materials and methodology

HPTE is a computer-controlled machine (W. Klement GmbH, Austria) [35] consisting of one upper die, one lower die, and a punch that extrudes the samples at a constant speed v. The upper die is fixed while the lower die is attached to an electromotor by a chain and rotates with a rotational speed ω (see Fig. 1).

The equivalent Von Mises strain imposed by HPTE in each pass of extrusion can be obtained by equation (1), [35].

$$\bar{\varepsilon}_{\text{HPTE}} = 2ln\frac{D1}{D0} + 2ln\frac{D1}{D2} + \frac{2\pi \bullet \omega \bullet R \bullet D1}{\sqrt{3} \bullet v \bullet D2} \qquad \text{Equ. (1)}$$

where D_0, D_1, and D_2 are the diameters of the extrusion channel in the upper die, the deformation zone, and the lower die, respectively; these values are fixed ($D_0 = 12$ mm, $D_1 = 14$ mm and $D_2 = 10.6$ mm). R is the distance from the die center at the cross section of the sample. As can be seen in equation (1), the only variables are the extrusion speed (v) and rotational speed (ω), and they are controlled by the computer. Further information about the die design and the process parameters can be found elsewhere [35,36]. Deformation of materials in HPTE results from the combination of shear/torsion and expansion/extrusion. Consequently, there is a gradient distribution of strain at the cross section of the samples [37,38].

In this set of experiments, the specimens were extruded with extruding speeds of $v = 7$ and 10 (mm/min), and the lower die was simultaneously rotating with an angular speed of $\omega = 1$ (rpm). Depending on the process parameters and the distance from the die center, different levels of strain were induced in the material. Table 1
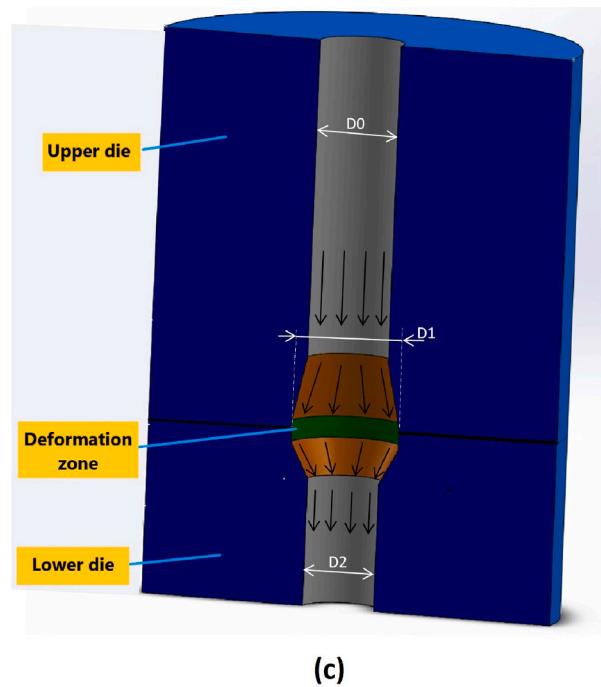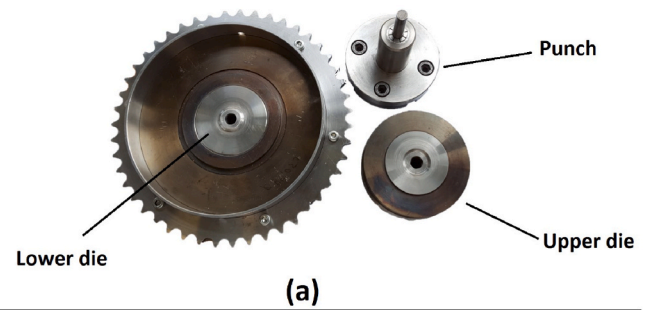

(a)

(b)

(c)

Fig. 1. HPTE die; (a) die components; (b) assembled configuration; (c) 3D demonstration of the cross section of the die.

Table 1
Equivalent Von Mises strain induced by HPTE after one pass of extrusion. R is the distance from the centerline.

		R [mm]	0.9	1.8	2.7	3.6	4.5
Equivalent strain	HPTE v10		1.3	1.7	2.2	2.6	3.0
	HPTE v7		1.5	2.1	2.7	3.3	3.9

presents the strain at different locations in the cross section of the samples.

As received niobium with a purity of 99.5 wt% was cut into billets of 11.8 mm in diameter and 35 mm in length. The specimens were extruded by HPTE at room temperature, and molybdenum disulphide (MoS_2) was used as a lubricant for the extrusion process. The sample preparation of the surfaces started with mechanical polishing using SiC abrasive papers up to 4000 grits and then continued with 5, 3, and 1 μm aluminum oxide suspensions. The polishing process was completed by using a 60 nm diamond paste to obtain a mirror surface. The EBSD analysis was performed at the edge zone of the samples at a distance of ~ R = 4.5 mm from the center of the disk by using a Bruker Esprit-2.1, operating at 20 kV. Orientation Imaging Microscopy (OIM) software was used for the analysis of the EBSD results, and a 15° criterion was employed to differentiate between the low-angle boundaries (LAGBs) and high-angle boundaries (HAGBs). Using OIM software, the area fraction of the grains was constructed, and the area-weighted mean grain size was determined. The x-ray diffraction (XRD) patterns were obtained using a Bruker D8 Focus with Cu Ka radiation (λ = 1.5406 Å), and the patterns were analyzed by the Topas software [39].

A SHIMATZU HMW micro-hardness tester was implemented to measure the microhardness. The micro indenter applied a load of 200 gr-force with a dwelling time of 15 s to the points on the cross section of the samples.

Hydrogenation of the specimens was conducted using a homemade Sievert apparatus with calibrated volumes to measure the kinetics of absorption. Specimens were cut into small chunks of ~100 mg and then exposed to hydrogen gas in a reactor at a constant pressure of 20 bar at 300 °C.

3. Results and discussion

3.1. Analysis of the microstructure

Fig. 2 shows the crystallographic orientation maps from the cross section of the samples in the edge zone. The distribution of the grain size and misorientation angles are presented in the histograms of Fig. 3. These results show that the as-received sample with an average grain size of 16.5 μm experienced a substantial microstructural refinement, and an average grain size of 2.2 μm in HPTE-v10, and 600 nm in HPTE-v7 were obtained. Furthermore, the results of EBSD analysis suggest that a large fraction of high-angle grain boundaries (HAGBs) formed in the microstructure after processing. The volume fraction of HAGBs in the as-received sample from the initial value of 51 % turned to 80 % in HPTE-v10 and to 91 % in HPTE-v7 which may imply that HPTE was able to fabricate materials with a predominant HAGB-microstructure. It has been evidenced that HAGBs -as opposed to low-angle grain boundaries (LAGBs)- have a stronger contribution to interfering with the slip process, hindering the dislocation movement, and thus improving the mechanical properties of the material [40]. Results of hardness testing agreed with this fact (see Fig. 4).

According to the results of Vickers hardness testing, the initial hardness of 82 HV increased to the hardness values of 236 HV and to 284 HV at the edge zones of HPTE-v10 and -v7, which indicate 2.8 and 3.5 times increase, respectively. The effect of torsional strain on the cross section of the samples is also visible; the as-received sample showed no major variation in hardness whereas the processed samples presented a gradual increase in hardness from center to edge.

X-ray diffraction (XRD) analysis was performed on the samples and the results were studied by Rietveld refinement to evaluate the evolution of the crystal structure and to measure the crystallite size (T) and microstrain (ε). Fig. 5 shows the Rietveld refinement of the patterns obtained from the samples HPTE-v7 and v10.

Using the estimated values of T and ε, the amount of dislocation density (ρ) in the samples can be calculated by Equation (2), [41,42].
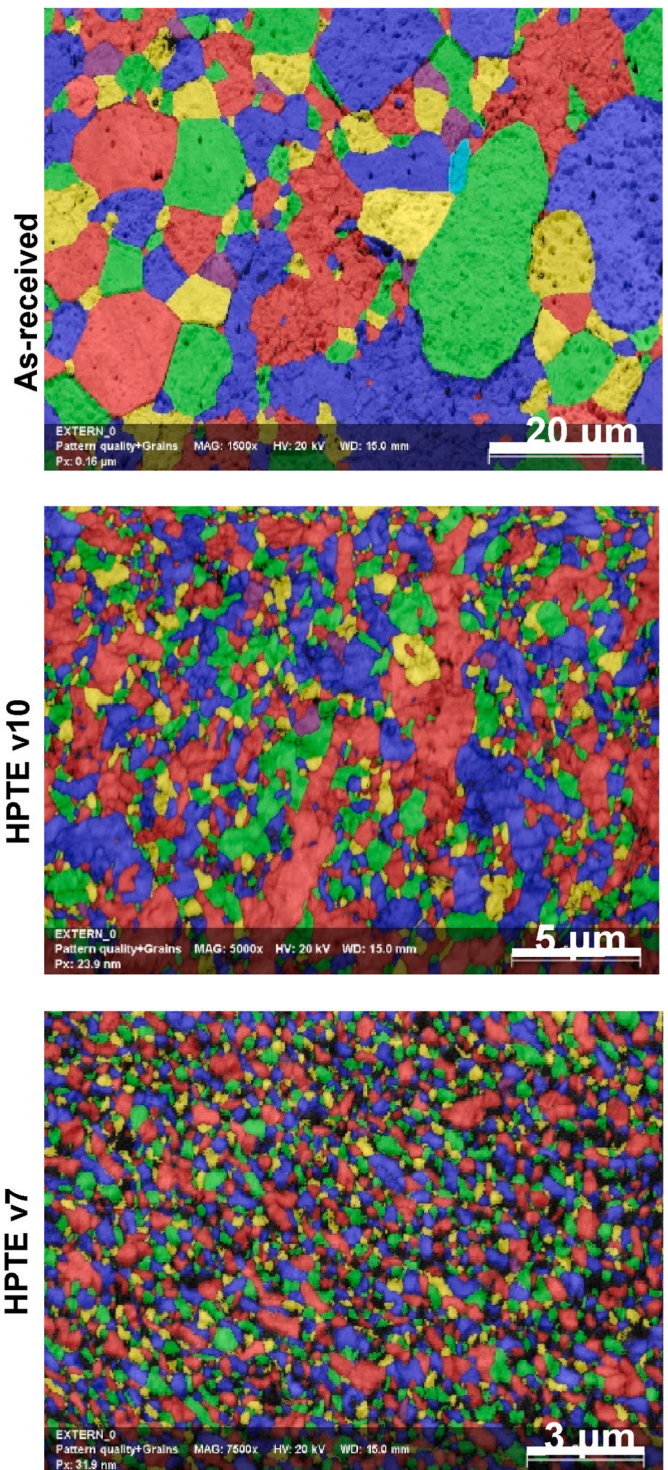

Fig. 2. Crystallographic orientation maps taken from the cross section of the samples before and after HPTE.

$$\rho = \frac{2\sqrt{3}\varepsilon^2}{\tau \times b} \qquad \text{Equ.(2)}$$

In this equation, b is the burgers vector and can be expressed as $b = \frac{\sqrt{3}}{2}a$ for BCC crystal structures [43], where "a" is the lattice parameter. Thus, the burgers vector for niobium is b_{Nb} = 0.285 nm. By substituting all parameters in Equation (2), the amount of dislocation density was measured as shown in Table 2.
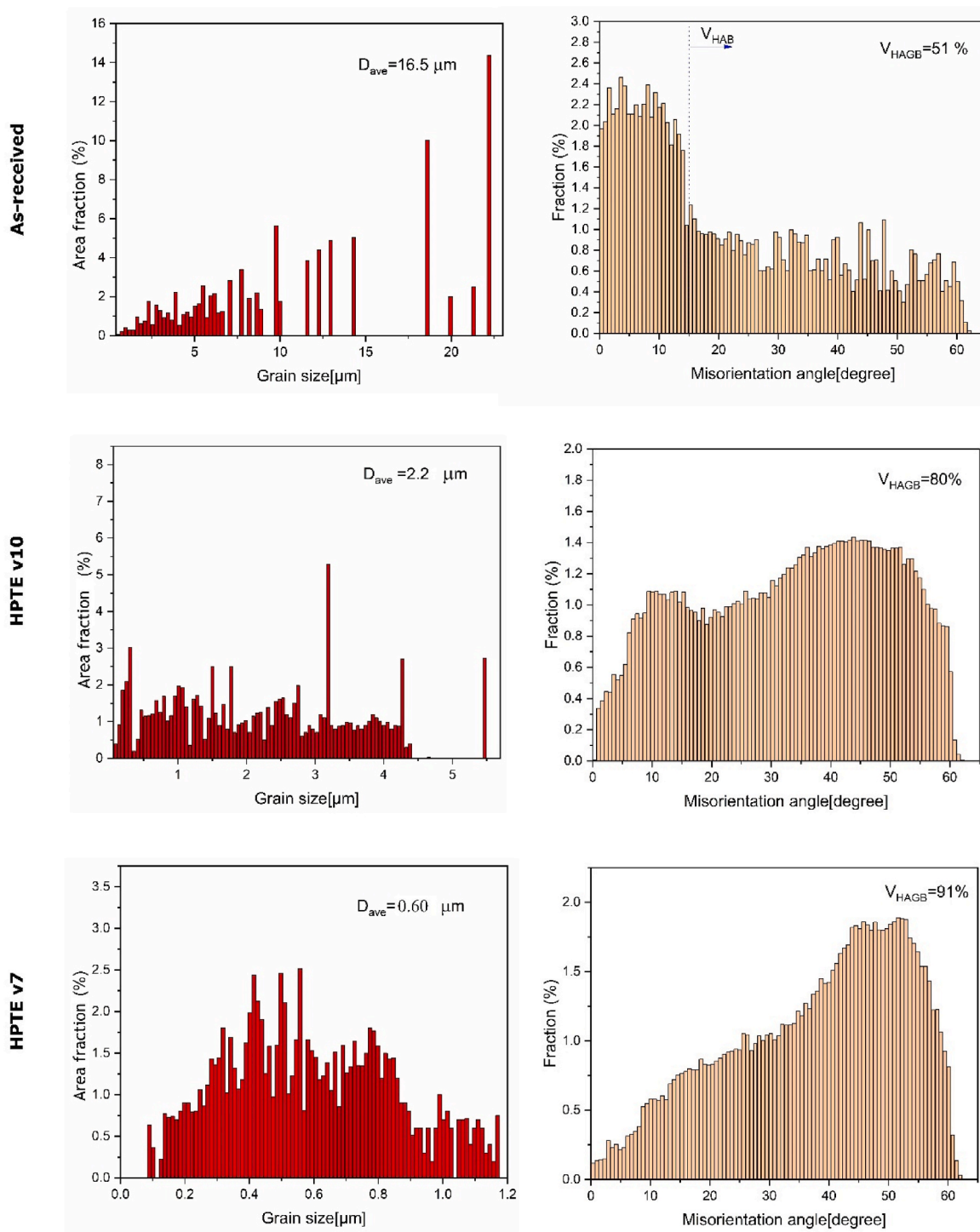
Fig. 3. Distribution of the grain size (left) and grain-boundary misorientation angles (right) obtained from EBSD analysis.

In accordance with the results of EBSD, the crystallite-size values obtained by XRD analysis also presented a descending order by imposing further strain on the material. All structural parameters of the samples along with the results of EBSD and hardness testing are shown in Table 2.

As shown in this table, the as-received sample presented the biggest grain size, the biggest crystallite size, and the lowest HAGB% with no microstrain. In addition, the microhardness of the sample was the lowest. The HPTE samples, on the other hand, demonstrated smaller grain size and crystallite size with a higher percentage of HAGBs as well as higher values of hardness depending on the amount of deformation they received.

3.2. Hydrogenation kinetics

Kinetics of the first hydrogenation (activation) measured by the Sievert apparatus are shown in Fig. 6. By considering the maximum capacity of niobium as 0.84 wt% [44], the as-received sample was not able to absorb hydrogen after one day of exposure whereas the other two processed samples absorbed hydrogen, demonstrating the influence of HPTE on the enhancement of activation. In the case of HPTE-v10, the sample was partially activated up to 80 % of the capacity after one day of
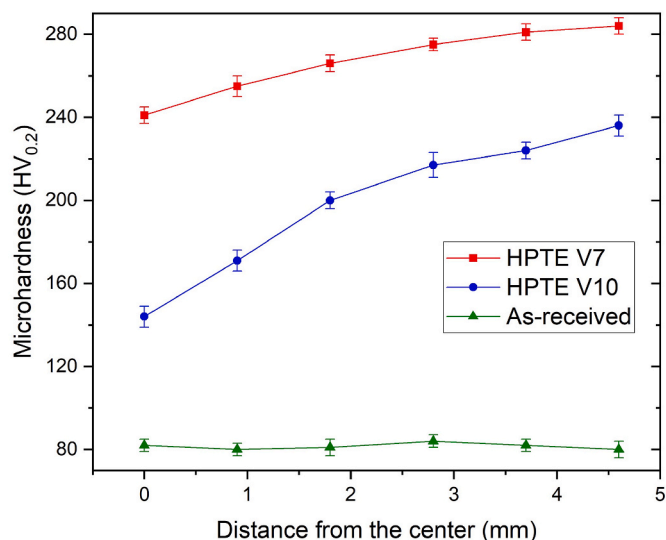
Fig. 4. Distribution of hardness across the cross section of the samples from center to edge.

exposure, while the other sample (HPTE-v7) which received a higher amount of deformation (see Table 1) reached the full capacity within ~6 h.

Enhancing the kinetics of the first hydrogenation by SPD processing of metals and alloys has been reported extensively. More attempts have been made recently to develop new techniques for the enhancement of properties in metals such as Twin Parallel Channel Angular Extrusion (TPCAE) [45], Accumulative fold forging [46], fast forging [47], etc. In this work, we showed that HPTE processing could refine the microstructure, improve the mechanical properties, and facilitate the diffusion of hydrogen in niobium, resulting in accelerating the activation of the material. However, the mechanism of hydrogen sorption and the effect of HPTE on the mechanism of absorption have not been understood yet.

3.3. Analysis of the mechanism of absorption

In general, the mechanism of hydrogen absorption is composed of different steps including hydrogen dissociation, penetration, diffusion, hydride formation and growth [48]. The slowest part of these reactions is a crucial bottleneck which determines the rate of the reaction and is called the rate limiting step [49] or rate determining step [50]. Different rate limiting step models have been developed to predict the mechanism of hydrogen sorption and to represent the hydrogen uptake ratio (X = % H_{abs}/%H_{max}). To comprehend the influence of HPTE on the absorption mechanism, several rate limiting step models were implemented here to study the mechanism of absorption during the first hydrogenation: Chemisorption (X), the simplest model, is based on the surface reaction which defines the hydride fraction proportional to the amount of reactant, and thus, linearly proportional to the time [51]. Johnson-Mehl-Avrami 2-dimensional (JMA-2D) and 3-dimensional (JMA-3D) describe the hydride phase formation based on nucleation and growth on the surface and inside the particles at a constant velocity [52,53]. Eventually, the geometrical contraction-based models, Contracting Volume −2 dimensional and −3 dimensional (CV2D & CV3D) [54,55] and Ginstling-Brounshtein 2-dimensional and 3-dimensional (GB2D & GB3D) [56,57] that represent a rapid hydride formation on the surface of a particle followed by growth into the center; when the metal/hydride interface motion is assumed to be at a constant velocity in CV models and at a decreasing velocity in GB models [58]. Table 3 describes each model and the corresponding equation. The best model shall fit the experimental data and can be representative of the reaction mechanism.

Fig. 7 shows the linear regression of the rate limiting step models described in Table 3 for the samples HPTE-v7 and HPTE-v10. The vertical axis in this graph represents the left side of the equations in the table and the slope of the lines is the kinetics rate constant (k). The as-received sample was excluded from the regression analysis since it did not absorb hydrogen at all.

It is commonly accepted that the rate limiting step model is applied to a range of X = 10 % to 80 % or 90 % of the reaction completion [49, 61–64] to exclude the uncertainty at the early stage and the late stage of the reaction [48] because the kinetics at these transient periods are not stable and hence, the results would be outliers in the linear regression. In this study, the HPTE-v7 sample completed the reaction within a short time frame and therefore, the range of X = [10−90]% was selected for the regression analysis. However, in the case of HPTE-v10, since the sample was not able to reach full capacity, a range of X = [10−100]% was adopted for this sample.

In order to find the best model, the adjusted R-squared values (R^2) of the regression models were measured and collected in Table 4. This parameter represents the accuracy of the model or in other words, the goodness of fit [65]; as such, when R^2 equals 1, the model perfectly fits the data. As shown in this table, the GB2D and GB3D models in HPTE-v7, and the CV3D and GB3D models in HPTE-v10 presented the highest R-squared values ($R^2 > 0.99$).

Nevertheless, the aforementioned models have similar R^2 values up to two decimal digits. For further inspection of the curves and the analysis of the goodness of models, residual values of the regressions for those of $R^2 \geq 0.99$ (highlighted in Table 4) were analyzed and plotted in Fig. 8. Residuals in regression analysis show the difference between the fitted curve and the experimental data. In linear regression, a residual value of zero indicates that the model fully aligns with the observed data and vice versa [66]. A good residual curve should have constant variance, i.e. the predicted values are randomly scattered around zero and the mean value of the residuals shall approach zero [65].

3.4. Comparison of the models

In principle, the chemisorption model (or surface reaction model; see Table 3) assumes that the transformed fraction of the new phase (X) is linearly proportional to the time (t); the slowest part of the hydrogenation in this model is the surface reaction of the metal with hydrogen when a dissociation or recombination of hydrogen molecules occurs [61]. This model is far from the real hydrogenation reactions that occurred in the HPTE-processed samples here (low R^2 values; see Table 4). The JMA model suggests that the nucleation and growth of the new phase can start randomly on the surface or the bulk and that the diffusion is rather fast [51]. By considering the R^2 values presented in Table 4, it seems that this model can predict the hydrogenation reaction better than the chemisorption model, but still not the best model. The contracting volume (C.V) proposes that nucleation starts quickly on the surface of the particles and then grows into the bulk [60,67]. According to this model, the rate limiting step in hydrogen diffusion is the interface velocity [60,67]. Based on the results of Table 4, the 3-dimensional modelling of C.V. (CV3D) has an accurate prediction of the hydrogen sorption behavior in the v10 sample ($R^2 > 0.99$). The Ginstling-Brounshtein (GB) model can accurately describe the diffusion kinetics of hydrogenation in spherical particles [56,68]. It assumes that a spherical particle reacts with a substance, the entire surface of the particle takes part in the reaction, and the particle radius will not change during the reaction [56,68]. The GB model has been basically used for describing the diffusion mechanisms in the solid-state synthesis of different materials such as Portland cement, magnesium ferrites, carbohydrate polymers, braided carbon fibers, epoxy resin [69], and metal hydrides [70]. In this study, the implementation of the 3-dimensional GB (GB3D) presented precise modelling in the case of the HPTE-v7 sample with the $R^2 > 0.99$ (see Table 4); further analysis of GB3D
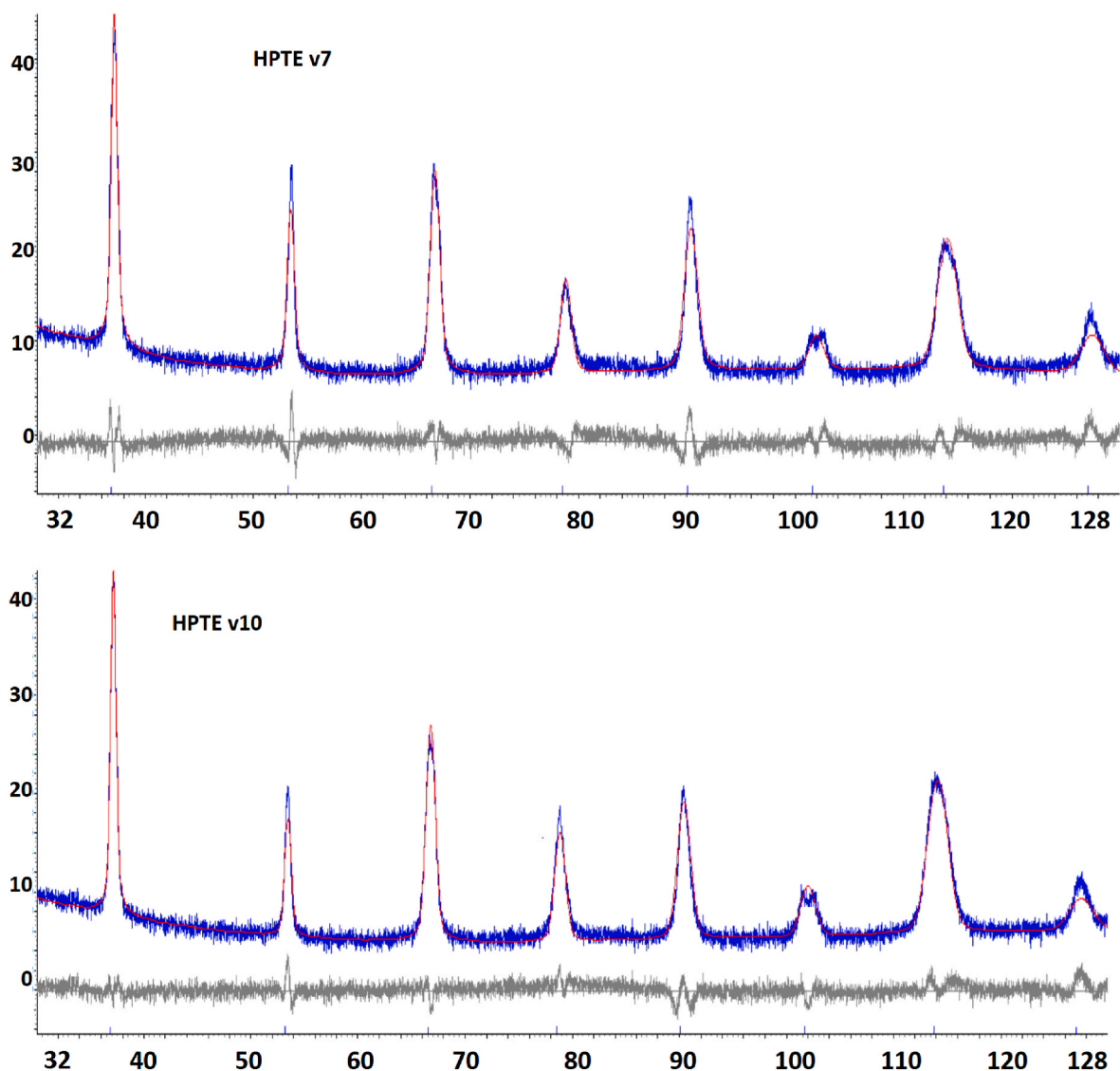
Fig. 5. Rietveld refinement of XRD patterns for HPTE-v7 and -v10. The blue line represents the measured patterns; the red line (overlapped with the blue one) reflects the calculated patterns, and the gray one shows the residue. (For interpretation of the references to colour in this figure legend, the reader is referred to the Web version of this article.)

Table 2
Structural parameters of the samples: Grain size and High Angle Grain Boundary fractions (HAGB %) were obtained by EBSD from the edge of the samples, microhardness by Vickers tester from the edge, crystallite size and microstrain by Rietveld refinement. The numbers in parentheses indicate the error on the last significant digit(s).

	Area-weighted mean grain size (μm)	HAGB %	Max microhardness (HV)	Crystallite size, d (nm)	Microstrain, ε (%)	Dislocation density, ρ (10^{14} m^{-2})
As received	16.5(10)	51	80(4)	43.9(3)	–	–
HPTE v10	2.2(4)	80	236(7)	39.8(2)	0.198(2)	6.1(6)
HPTE v7	0.6(1)	91	284(8)	27.5(4)	0.209(1)	9.3(8)

model by residuals confirms this fact since the residual curve is fairly distributed around the zero axis; see Fig. 8.

Indeed, the hydrogenation kinetics of V7 and V10 showed that the kinetics of absorption in v10 was much slower than that of v7, and the hydrogenation reaction in v10 was not complete (see Fig. 6). A comparison of the rate limiting step models of CV3D, GB2D, and GB3D for the samples revealed that these models are the most suitable ones to show the mechanism of hydrogen sorption. However, the analysis of the R^2 values together with residuals may help to choose the best model among them. In the case of the v7 sample, the GB2D and GB3D models presented the highest R^2 value, but the residuals were slightly different.

According to Fig. 8-a, the residual curve in GB3D had less variation around zero and thereby, represented the best-predicting model in the hydrogen sorption of the v7 sample. This means that the hydrogenation mechanism in this sample was based on a 3-dimensional growth of the hydride phase with decreasing interface velocity. On the other hand, in the v10 sample, the two models CV3D and GB3D, presented the highest R^2 values. Comparison of the residual curves reveals that from the beginning of the synthesis near to the end, the residual curves were similar (distributed around the zero axis) although in the last steps of the activation, the residual values of the CV3D model went far away from the zero axis while the GB3D model showed a lower variation in
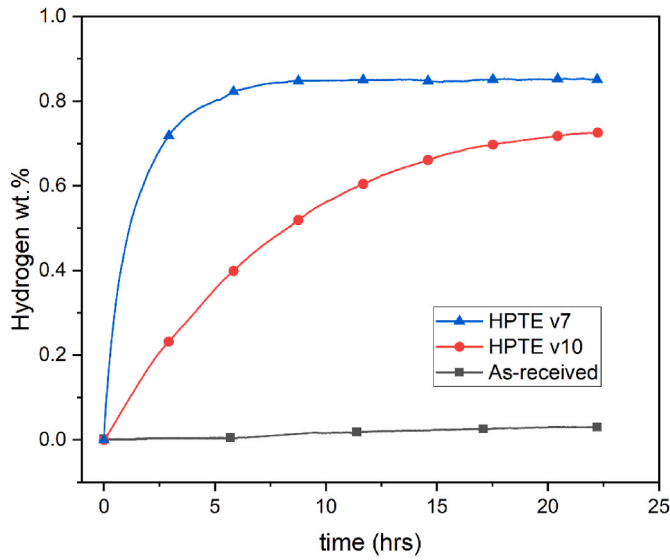
Fig. 6. Kinetics of activation in processed and as-received specimens.

Table 3

Rate limiting step models. The left side of the equation in all cases is a function of the hydrogenation completion ratio (X = %H$_{abs}$/%H$_{max}$), and on the right side, t is the reaction time and k is the kinetic rate constant.

Model	Mathematical equation	Description
Chemisorption (X)	$X = kt$ [51]	Surface controlled interaction
JMA2D	$[-\ln(1-X)]^{\frac{1}{2}} = kt$ [59]	2D growth of the existing nuclei with constant interface velocity
JMA3D	$[-\ln(1-X)]^{\frac{1}{3}} = kt$ [60]	3D growth of the existing nuclei with constant interface velocity
CV2D	$1 - (1-X)^{\frac{1}{2}} = kt$ [54]	2D growth of the interface with constant velocity
CV3D	$1 - (1-X)^{\frac{1}{3}} = kt$ [55]	3D growth of the interface with constant velocity
GB2D	$(1-X)\ln(1-X) + X = kt$ [56]	Diffusion-controlled 2D growth of the interface with decreasing velocity
GB3D	$1 - \left(\frac{2X}{3}\right) - (1-X)^{\frac{2}{3}} = kt$ [56]	Diffusion-controlled 3D growth of the interface with decreasing velocity

Fig. 7. Linear regression of rate limiting step models for the samples HPTE -v7 and -v10. The experimental results (illustrated in points) were adopted from Fig. 6. The description of each model is presented in Table 3.

Table 4

Adjusted R^2 value obtained from the regression analysis.

Model	Adjusted R^2 value	
	V7	V10
X	0.8871	0.8640
JMA2D	0.9539	0.9898
JMA3D	0.9262	0.9819
CV2D	0.9589	0.9781
CV3D	0.9758	0.9960
GB2D	0.9935	0.9854
GB3D	0.9985	0.9949

residuals. (see Fig. 8-b). Thus, it can be concluded that GB3D is the most suitable one for demonstrating the hydrogen sorption behavior of the two HPTE-processed samples although, in the case of v10, both CV3D and GB3D can fairly represent the absorption mechanism.

The slight difference between the hydrogen absorption mechanisms in the two samples can be explained by the difference in the microstructural features of each one. Usually, the chemical reactions in metals (including hydrogenation) start with nucleation either on the grain boundaries or crystalline defects [71]. As demonstrated earlier in Fig. 2 & Table 2, the HPTE-v7 sample possessed the highest level of dislocation density as well as the finest microstructure. This means that nucleation points in the v7 sample should be much more than those of the v10 sample. Hence, the nucleation points are close to each other, and the expanding boundary of the hydride phase might disrupt the progress of an adjacent hydride phase, resulting in a reduced growth rate. Thus, because of such interference, the rate limiting step in the v7 sample is decreasing interface velocity (GB3D). In the other sample, v10, the nucleation points of the hydride phase are far from each other, and they do not interfere with the neighboring hydride phase when growing. Consequently, they can grow with constant velocity without restrictions (CV3D model). At some point, however, the boundaries of the new
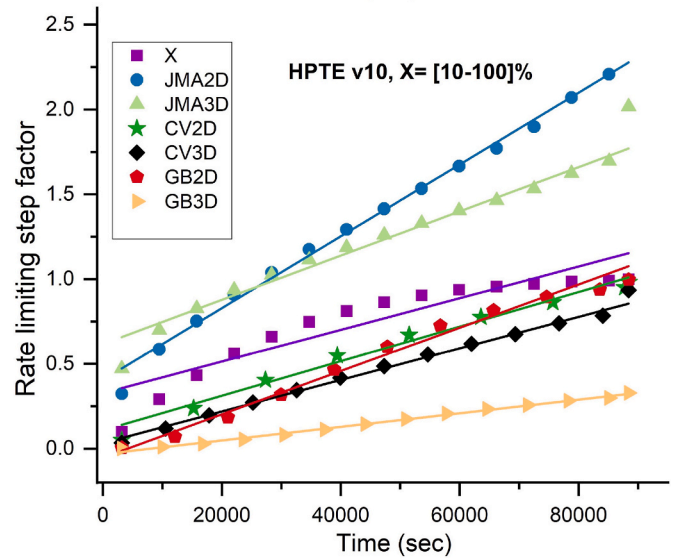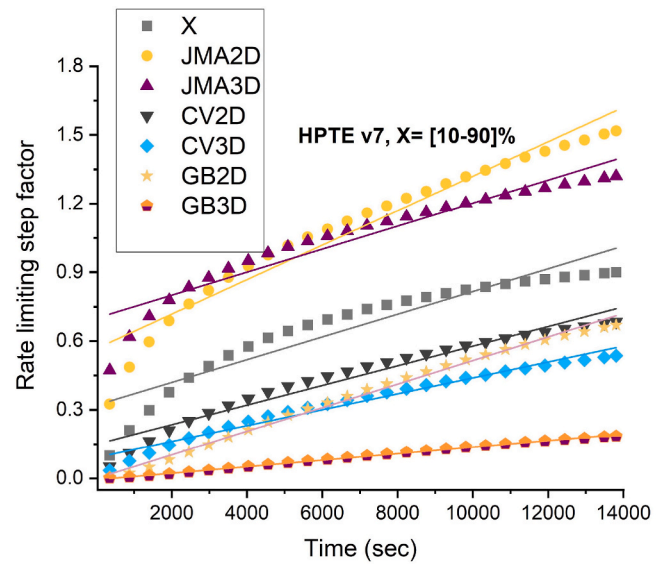
phases may interfere with each other and the velocity of the growing interface will decrease suggesting that the rate limiting step will change to the decreasing interface velocity (GB3D). Generally, the CV models, (CV2D and CV3D) are best when the growth of the interface is at a constant velocity contrary to the GB models (GB2D and GB3D) when the interface is growing with a decreasing velocity.
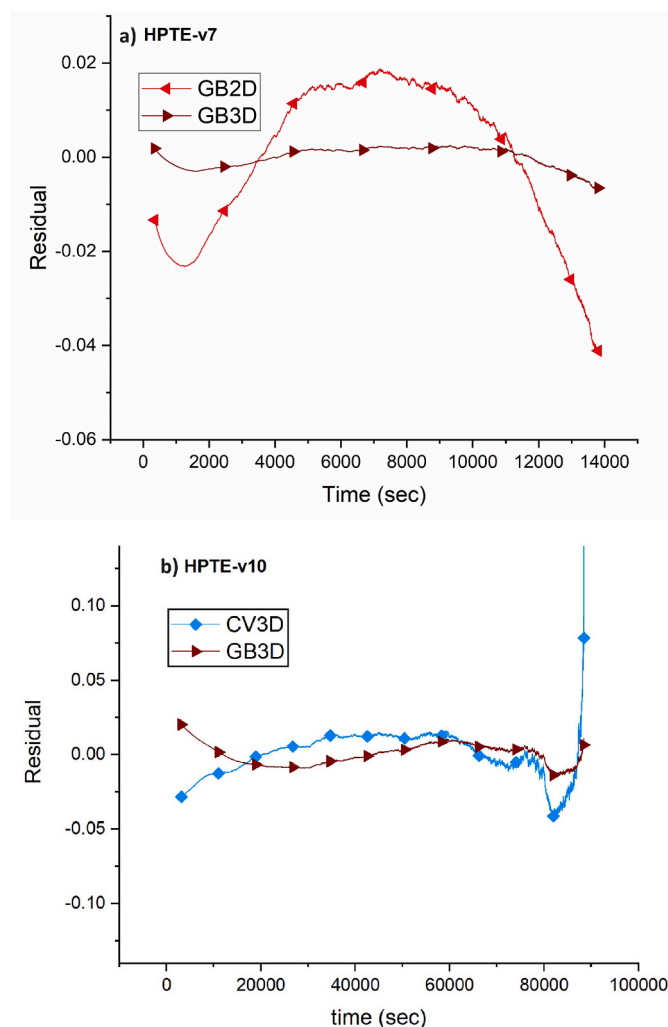
Fig. 8. Residual curves for the linear regression of the rate limiting step modelling.

It is worth mentioning that in this study, both models of CV3D and GB3D demonstrated reasonably high R-squared values when predicting the absorption mechanisms in the v10 sample. However, in the final stages, the GB3D model proved to be superior in modelling the hydrogenation mechanism. It is also important to highlight that this research studied the mechanism of hydrogen sorption in the HPTE-processed samples for the first time; more investigations seem to be necessary to better understand the impact of this technique on the mechanism of hydrogenation in metal hydrides. Further investigations are underway to assess the effect of HPTE and its process parameters on the H-sorption properties of other materials.

4. Conclusion

We evaluated a new mechanical nanostructuring technique for the synthesis of metal hydrides -called High Pressure Torsion Extrusion (HPTE). Two different extrusion speeds of v = 7 mm/min and v = 10 mm/min in HPTE were implemented to synthesize niobium. The results of this study proved that HPTE was effective in the microstructural refinement of the material, thus, enhancing the mechanical properties as well as the kinetics of the first hydrogenation.

The initial grain size of 16.5 μm in the as-received sample was reduced to 600 nm just in one pass of extrusion in the HPTE-v7 regime; a large volume of dislocation densities accumulated in the samples, and an increase in the fraction of high-angle grain boundaries appeared after

processing. As a result, a noticeable improvement in hardness was achieved.

The enhancement in the first hydrogenation (activation) depended on the HPTE regime and the amount of deformation applied to the material. The initial sample (as-received) was not able to absorb hydrogen after one day of exposure to the hydrogen gas while the HPTE-processed samples were able to be activated and absorb hydrogen. The HPTE-v10 sample was partially activated up to ~80 % of the capacity in one day, while the HPTE-v7 sample (which received a higher amount of deformation) was activated to full capacity within ~6 h.

A linear regression analysis of the rate limiting step of the hydrogenation synthesis showed that the absorption mechanism in the HPTE samples is governed by the 3-dimensional diffusion of hydrogen following the Ginstling-Brounshtein model (GB3D) in HPTE-v7, and a combination of contracting volume (CV3D) and Ginstling-Brounshtein (GB3D) in HPTE-v10.

References

[1] Zhang J, Yao Y, He L, Zhou XJ, Yu LP, Lu XZ, et al. Hydrogen storage properties and mechanisms of as-cast, homogenized and ECAP processed Mg98.5Y1Zn0.5 alloys containing LPSO phase. Energy 2021;217. https://doi.org/10.1016/J.ENERGY.2020.119315.
[2] Khayrullina AG, Blinov D, Borzenko V. Novel kW scale hydrogen energy storage system utilizing fuel cell exhaust air for hydrogen desorption process from metal hydride reactor. Energy 2019;183:1244–52. https://doi.org/10.1016/J.ENERGY.2019.07.021.
[3] Kumar S, Tiwari GP, Sonak S, Jain U, Krishnamurthy N. High performance FeTi - 3.1 mass % V alloy for on board hydrogen storage solution. Energy 2014;75:520–4. https://doi.org/10.1016/j.energy.2014.08.011.
[4] Schlapbach L, Züttel A. Hydrogen-storage materials for mobile applications. Nature 2001;414:353–8. https://doi.org/10.1038/35104634.
[5] Lv P, Huot J. Hydrogenation improvement of TiFe by adding ZrMn2. Energy 2017;138:375–82. https://doi.org/10.1016/j.energy.2017.07.072.
[6] Alam MM, Sharma P, Huot J. On the hydrogen storage properties of cast TiFe mechanically milled with an intermetallic LaNi5 and rare-earth elements La and Ce. Int J Hydrogen Energy 2023. https://doi.org/10.1016/J.IJHYDENE.2023.08.100.
[7] Liu L, Ilyushechkin A, Liang D, Cousins A, Tian W, Chen C, et al. Metal hydride composite structures for improved heat transfer and stability for hydrogen storage and compression applications. Inorganics 2023;11:181. https://doi.org/10.3390/INORGANICS11050181. 2023;11:181.
[8] Godula-Jopek A, Jehle W, Wellnitz J. Storage of pure hydrogen in different states. Hydrogen Storage Technologies; 2012. p. 97–170. https://doi.org/10.1002/9783527649921.ch4.
[9] Cesario Asselli AA, Bourbeau Hébert N, Huot J. The role of morphology and severe plastic deformation on the hydrogen storage properties of magnesium. Int J Hydrogen Energy 2014;39:12778–83. https://doi.org/10.1016/j.ijhydene.2014.06.042.
[10] Huot J. Enhancing hydrogen storage properties of metal hybrides. Cham: Springer International Publishing; 2016. https://doi.org/10.1007/978-3-319-35107-0.
[11] Wang F, Li R, Ding C, Tang W, Wang Y, Xu S, et al. Enhanced hydrogen storage properties of ZrCo alloy decorated with flower-like Pd particles. Energy 2017;139:8–17. https://doi.org/10.1016/j.energy.2017.07.143.
[12] Rosochowski A. Severe plastic deformation technology, vol. 38. Whittles Publishing; 2017. https://doi.org/10.1016/j.jallcom.2003.10.065.
[13] Huot J, Ravnsbæk DB, Zhang J, Cuevas F, Latroche M, Jensen TR. Mechanochemical synthesis of hydrogen storage materials. Prog Mater Sci 2013;58:30–75. https://doi.org/10.1016/j.pmatsci.2012.07.001.
[14] Kocich R, Lukáč P. SPD processes - methods for mechanical nanostructuring. Handbook of mechanical nanostructuring. Weinheim, Germany: Wiley-VCH Verlag GmbH & Co. KGaA; 2015. p. 235–62. https://doi.org/10.1002/9783527674947.ch11.

[15] Rabkin E, Skripnyuk V, Estrin Y. Ultrafine-grained magnesium alloys for hydrogen storage obtained by severe plastic deformation. Front Mater 2019;6:1–9. https://doi.org/10.3389/fmats.2019.00240.

[16] Emami H, Edalati K, Staykov A, Hongo T, Iwaoka H, Horita Z, et al. Solid-state reactions and hydrogen storage in magnesium mixed with various elements by high-pressure torsion: experiments and first-principles calculations. RSC Adv 2016; 6:11665–74. https://doi.org/10.1039/c5ra23728a.

[17] Edalati K, Akiba E, Botta WJ, Estrin Y, Floriano R, Fruchart D, et al. Impact of severe plastic deformation on kinetics and thermodynamics of hydrogen storage in magnesium and its alloys. J Mater Sci Technol 2023;146:221–39. https://doi.org/10.1016/J.JMST.2022.10.068.

[18] Edalati K, Uehiro R, Fujiwara K, Ikeda Y, Li HW, Sauvage X, et al. Ultra-severe plastic deformation: evolution of microstructure, phase transformation and hardness in immiscible magnesium-based systems. Mater Sci Eng, A 2017;701: 158–66. https://doi.org/10.1016/j.msea.2017.06.076.

[19] Valiev RZ, Langdon TG. Principles of equal-channel angular pressing as a processing tool for grain refinement. Prog Mater Sci 2006;51:881–981. https://doi.org/10.1016/j.pmatsci.2006.02.003.

[20] Sahoo PS, Meher A, Mahapatra MM, Vundavilli PR. Understanding the fabrication of ultrafine grains through severe plastic deformation techniques: an overview. JOM 2022;74:3887–909. https://doi.org/10.1007/s11837-022-05442-6.

[21] Kommel L, Põdra P, Mikli V, Omranpour B. Gradient microstructure in tantalum formed under the wear track during dry sliding friction. Wear 2021;466–467: 203573. https://doi.org/10.1016/j.wear.2020.203573.

[22] Shahreza BO, Hernandez-Rodriguez MAL, Garcia-Sanchez E, Kommel L, Sergejev F, Salinas-Rodríguez A, et al. The impact of microstructural refinement on the tribological behavior of niobium processed by Indirect Extrusion Angular Pressing. Tribol Int 2021;167:107412. https://doi.org/10.1016/j.triboint.2021.107412.

[23] de Rango P, Fruchart D, Aptukov V, Skryabina N. Fast Forging: a new SPD method to synthesize Mg-based alloys for hydrogen storage. Int J Hydrogen Energy 2020; 45:7912–6. https://doi.org/10.1016/J.IJHYDENE.2019.07.124.

[24] Novelli M, Edalati K, Itano S, Li HW, Akiba E, Horita Z, et al. Microstructural details of hydrogen diffusion and storage in Ti–V–Cr alloys activated through surface and bulk severe plastic deformation. Int J Hydrogen Energy 2020;45: 5326–36. https://doi.org/10.1016/j.ijhydene.2019.07.058.

[25] Zhilyaev AP, Langdon TG. Using high-pressure torsion for metal processing: fundamentals and applications. Prog Mater Sci 2008;53:893–979. https://doi.org/10.1016/j.pmatsci.2008.03.002.

[26] Huot J. Cold rolling. SpringerBriefs in Applied Sciences and Technology; 2016. p. 27–38. https://doi.org/10.1007/978-3-319-35107-0_6.

[27] Beygelzimer Y, Varyukhin V, Synkov S, Orlov D. Useful properties of twist extrusion. Mater Sci Eng, A 2009;503:14–7. https://doi.org/10.1016/J.MSEA.2007.12.055.

[28] Kommel L, Shahreza BO, Mikli V. Microstructure and physical-mechanical properties evolution of pure tantalum processed with hard cyclic viscoplastic deformation. Int J Refract Metals Hard Mater 2019;83:104983. https://doi.org/10.1016/j.ijrmhm.2019.104983.

[29] Kommel L, Huot J, Shahreza BO. Effect of hard cyclic viscoplastic deformation on the microstructure, mechanical properties, and electrical conductivity of Cu-Cr alloy. J Mater Eng Perform 2022. https://doi.org/10.1007/s11665-022-06997-w.

[30] Pardis N, Talebanpour B, Ebrahimi R, Zomorodian S. Cyclic expansion-extrusion (CEE): a modified counterpart of cyclic extrusion-compression (CEC). Mater Sci Eng, A 2011;528:7537–40. https://doi.org/10.1016/j.msea.2011.06.059.

[31] Nugmanov D, Mazilkin A, Hahn H, Ivanisenko Y. Structure and tensile strength of pure Cu after high pressure torsion extrusion. Metals 2019;9:1–17. https://doi.org/10.3390/met9101081.

[32] Omranpour B, Ivanisenko Y, Kulagin R, Kommel L, Garcia Sanchez E, Nugmanov D, et al. Evolution of microstructure and hardness in aluminum processed by high pressure torsion extrusion. Mater Sci Eng 2019;762:138074. https://doi.org/10.1016/j.msea.2019.138074.

[33] Omranpour B, Kommel L, Garcia Sanchez E, Ivanisenko J, Huot J. Enhancement of hydrogen storage in metals by using a new technique in severe plastic deformations. Key Eng Mater 2019;799:173–8. KEM, Trans Tech Publications, https://doi.org/10.4028/www.scientific.net/KEM.799.173.

[34] Huot J, Pelletier JF, Lurio LB, Sutton M, Schulz R. Investigation of dehydrogenation mechanism of MgH2-Nb nanocomposites. J Alloys Compd 2003;348:319–24. https://doi.org/10.1016/S0925-8388(02)00839-3.

[35] Yu Ivanisenko, Kulagin R, Fedorov V, Mazilkin A, Scherer T, Baretzky B, et al. High Pressure Torsion Extrusion as a new severe plastic deformation process. Mater Sci Eng, A 2016;664:247–56. https://doi.org/10.1016/j.msea.2016.04.008.

[36] Omranpour B, Kulagin R, Ivanisenko Y, Garcia Sanchez E. Experimental and numerical analysis of HPTE on mechanical properties of materials and strain distribution. IOP Conf Ser Mater Sci Eng 2017;194:012047. https://doi.org/10.1088/1757-899X/194/1/012047. IOP Publishing.

[37] Omranpour B, Ivanisenko Y, Kulagin R, Kommel L, Garcia Sanchez E, Nugmanov D, et al. Evolution of microstructure and hardness in aluminum processed by high pressure torsion extrusion. Mater Sci Eng 2019;762. https://doi.org/10.1016/j.msea.2019.138074.

[38] Omranpour B, Kommel L, Sergejev F, Ivanisenko J, Antonov M, Hernandez-Rodriguez MAL, et al. Tailoring the microstructure and tribological properties in commercially pure aluminium processed by High Pressure Torsion Extrusion. Proc Est Acad Sci 2021;70:540. https://doi.org/10.3176/proc.2021.4.23.

[39] Liu J, Xu J, Sleiman S, Chen X, Zhu S, Cheng H, et al. Microstructure and hydrogen storage properties of Ti–V–Cr based BCC-type high entropy alloys. Int J Hydrogen Energy 2021;46:28709–18. https://doi.org/10.1016/j.ijhydene.2021.06.137.

[40] Faraji G, Kim HS, Kashi HT. Effective parameters for the success of severe plastic deformation methods. Severe Plastic Deform. 2018;187–222. https://doi.org/10.1016/B978-0-12-813518-1.00006-0.

[41] Patra A, Saxena R, Karak SK. Combined effect of Ni and nano-Y2O3addition on microstructure, mechanical and high temperature behavior of mechanically alloyed W-Mo. Int J Refract Metals Hard Mater 2016;60:131–46. https://doi.org/10.1016/j.ijrmhm.2016.07.017.

[42] Tański T, Snopiński P, Prusik K, Sroka M. The effects of room temperature ECAP and subsequent aging on the structure and properties of the Al-3%Mg aluminium alloy. Mater Char 2017;133:185–95. https://doi.org/10.1016/j.matchar.2017.09.039.

[43] Li P, Lin Q, Wang X, Tian Y, Xue KM. Recrystallization behavior of pure molybdenum powder processed by high-pressure torsion. Int J Refract Metals Hard Mater 2018;72:367–72. https://doi.org/10.1016/j.ijrmhm.2018.01.002.

[44] Manchester FD, ASM International. Phase diagrams of binary hydrogen alloys. ASM International; 2000.

[45] Abdi M, Ebrahimi R, Bagherpour E. Improvement of hydrogenation and dehydrogenation kinetics of as-cast AZ91 magnesium alloy via Twin Parallel Channel Angular extrusion processing. Crystals 2022;12:1428. https://doi.org/10.3390/cryst12101428.

[46] Khodabakhshi F, Ekrt O, Abdi M, Gerlich AP, Mottaghi M, Ebrahimi R, et al. Hydrogen storage behavior of Mg/Ni layered nanostructured composite materials produced by accumulative fold-forging. Int J Hydrogen Energy 2022;47:1048–62. https://doi.org/10.1016/J.IJHYDENE.2021.10.096.

[47] de Rango P, Fruchart D, Aptukov V, Skryabina N. Fast Forging: a new SPD method to synthesize Mg-based alloys for hydrogen storage. Int J Hydrogen Energy 2020; 45:7912–6. https://doi.org/10.1016/J.IJHYDENE.2019.07.124.

[48] Park KB, Fadonougbo JO, Na TW, Lee TW, Kim M, Lee DH, et al. On the first hydrogenation kinetics and mechanisms of a TiFe0.85Cr0.15 alloy produced by gas atomization. Mater Char 2022;192. https://doi.org/10.1016/j.matchar.2022.112188.

[49] Lang J, Eagles M, Conradi MS, Huot J. Hydrogenation rate limiting step, diffusion and thermal conductivity in cold rolled magnesium hydride. J Alloys Compd 2014; 583:116–20. https://doi.org/10.1016/j.jallcom.2013.08.126.

[50] Kitagawa Y, Tanabe K. Development of a kinetic model of hydrogen absorption and desorption in magnesium and analysis of the rate-determining step. Chem Phys Lett 2018;699:132–8. https://doi.org/10.1016/J.CPLETT.2018.03.036.

[51] Mintz MH, Zeiri Y. Hydriding kinetics of powders. J Alloys Compd 1995;216: 159–75. https://doi.org/10.1016/0925-8388(94)01269-N.

[52] Avrami M. Granulation, phase change, and microstructure kinetics of phase change. III. J Chem Phys 2004;9:177. https://doi.org/10.1063/1.1750872.

[53] Avrami M. Kinetics of phase change. I general theory. J Chem Phys 2004;7:1103. https://doi.org/10.1063/1.1750380.

[54] Koga N, Criado JM. Kinetic analyses of solid-state reactions with a particle-size distribution. J Am Ceram Soc 1998;81:2901–9. https://doi.org/10.1111/J.1151-2916.1998.TB02712.X.

[55] Bösenberg U, Kim JW, Gosslar D, Eigen N, Jensen TR, von Colbe JMB, et al. Role of additives in LiBH4–MgH2 reactive hydride composites for sorption kinetics. Acta Mater 2010;58:3381–9. https://doi.org/10.1016/J.ACTAMAT.2010.02.012.

[56] Ginstling AM, Brounshtein BI. Concerning the diffusion kinetics of reactions in spherical particles. J Appl Chem USSR 1950;23:1327–38.

[57] Crank J. The mathematics of diffusion. second ed. 1975.

[58] Pang Y, Li Q. A review on kinetic models and corresponding analysis methods for hydrogen storage materials. Int J Hydrogen Energy 2016;41:18072–87. https://doi.org/10.1016/J.IJHYDENE.2016.08.018.

[59] Johnsson WA, Mehl RF. Reaction kinetics in processes of nucleation and growth. Trans Am Inst Min Metall Eng 1939;135:416–42.

[60] Avrami M. Kinetics of phase change. II transformation-time relations for random distribution of nuclei. J Chem Phys 2004;8:212. https://doi.org/10.1063/1.1750631.

[61] Barkhordarian G, Klassen T, Bormann R. Kinetic investigation of the effect of milling time on the hydrogen sorption reaction of magnesium catalyzed with different Nb2O5 contents. J Alloys Compd 2006;407:249–55. https://doi.org/10.1016/J.JALLCOM.2005.05.037.

[62] Lv P, Zhong C, Huang D, Zhou X, Liu Z, Huang D. Effect of introducing manganese as additive on microstructure, hydrogen storage properties and rate limiting step of Ti–Cr alloy. Int J Hydrogen Energy 2022;47:459–69. https://doi.org/10.1016/j.ijhydene.2021.10.029.

[63] Huang D, Lv P, Zhong C, Zhou X, Liu Z. Study on Hydrogen Storage Properties, Anti-Oxide Ability and Rate Limiting Step of ZrCr-Based Alloy after Introducing Cobalt as Additive n.d. https://doi.org/10.32604/jrm.2022.023261.

[64] Lv P, Zhong C, Huang D, Zhou X, Liu Z, Zhao R. Superior anti-impurity gas poisoning ability and hydrogen storage properties of Ti–Cr alloy by introducing zirconium as additive. Int J Hydrogen Energy 2022;47:18772–85. https://doi.org/10.1016/j.ijhydene.2022.04.041.

[65] George Casella, Berger R. Statistical inference. 2 nd. Duxbury Thomson Learning; 2002.

[66] Wheelan CJ, Davis J (Narrator), Brilliance Audio (Firm). Naked statistics : stripping the dread from the data [n.d].

[67] Avrami M. Granulation, phase change, and microstructure kinetics of phase change. III. J Chem Phys 2004;9:177. https://doi.org/10.1063/1.1750872.

[68] Brounshtein BI, Ginstling AM. Kinetics of the reaction of polydisperse mixtures of crystalline substances. J Appl Chem USSR 1956;29:2009–11.

[69] Krauklis AE, Dreyer I. A simplistic preliminary assessment of ginstling-brounstein model for solid spherical particles in the context of a diffusion-controlled synthesis. Open Chem 2018;16:64–72. https://doi.org/10.1515/chem-2018-0011.

[70] Patel AK, Duguay A, Tougas B, Neumann B, Schade C, Sharma P, et al. Study of the microstructural and first hydrogenation properties of TiFe alloy with Zr, Mn and V as additives. Processes 2021;9:1217. https://doi.org/10.3390/PR9071217. 2021; 9:1217.

[71] Huot J. Nanocrystalline metal hydrides obtained by severe plastic deformations. Metals 2012;2:22–40. https://doi.org/10.3390/met2010022.